FABRICATION OF QUADRANT-TYPE X-BAND SINGLE-CELL STRUCTURE USED FOR HIGH GRADIENT TESTS

Tetsuo Abe*, Yasuo Ajima, Yoshio Arakida, Toshiyasu Higo, Hitoshi Inoue, Noboru Kudo,
Shuji Matsumoto, Toshikazu Takatomi,
KEK, Tsukuba, Ibaraki 305-0801, Japan
Yasuo Higashi, OIST, Onna-son, Kunigami-gun, Okinawa 904-0495, Japan

Abstract

A most commonly used method to fabricate accelerating tubes is machining, followed by stacking of disks, and then bonding such as diffusion bonding and brazing. In accelerating structures fabricated with this kind of method, surface currents associated with magnetic fields flow across disk-to-disk junctions. On the other hand, we focus on a quadrant-type structure, where no surface currents flow across any junctions although naive such structures have some disadvantages. In this paper, based on our new ideas to overcome all of the disadvantages, we present a fabrication process of a quadrant-type X-band accelerating structure in the form of a single-cell test cavity [1], together with results on machining of quadrants and test of electron beam welding (EBW).

INTRODUCTION

High-gradient accelerating structures with gradients of ≈ 100 MV/m or higher are linchpins of high-energy accelerators to search for new physics in particle physics, and are also useful to make compact accelerators such as medical linacs. Most of such structures, made of oxygen free copper (OFC), have been fabricated so far by machining, followed by stacking of disks, and then bonding such as diffusion bonding and brazing (hereinafter referred to as disk-type). An example of the disk-type structures is shown in Fig. 1a. However, accelerating structures, fabricated with this kind of method, could have a potential problem that surface currents associated with magnetic fields (typically $\approx 10^8$ A/cm^2 during high-gradient operation) flow across disk-to-disk junctions, where perfect bonding of neighboring disks at the inner surface is not guaranteed. For example, in the report [2], there are gaps with some microscopic objects between the diffusion-bonded disks seen in the SEM images. Although we do not know the details of RF breakdown mechanism dominantly contributing to breakdown rates (BDRs) of accelerating structures, such defects should be deeply concerned because significant impact of surface magnetic field on BDRs has discovered [3, 4].

In this paper, based on the new ideas, we present a fabrication process of a quadrant-type X-band accelerating structure in the form of a single-cell test cavity, together with results on the machining of quadrants and EBW test. In single-cell structures, there are only three cells: a central cell to be tested (test cell), a matching cell, and an end
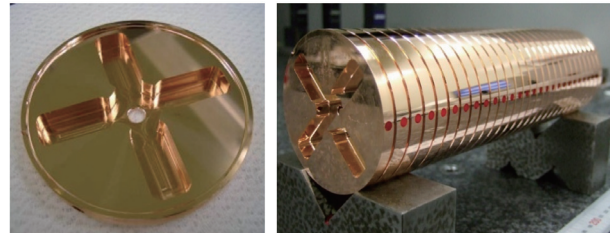
A damped disk   Disks stacked and bonded

(a) Example of the disk-type structures.
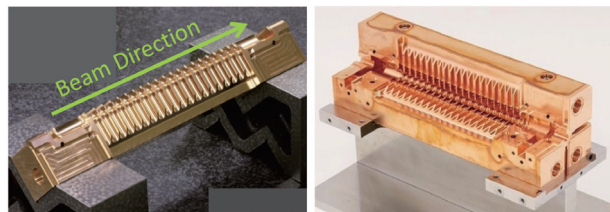
A quadrant   Three quadrants

(b) Example of the quadrant-type structures.

Figure 1: Two orthogonal methods to fabricate accelerating tubes.

cell, so that such structures are easier to make and test than multi-cell structures.

In this study, we focus on a fabrication method of quadrant-type structures as shown in Fig. 1b, where quadrants are machined with ultra-high precision milling, followed by bonding of quadrants. For quadrant-type structures, no surface currents associated with magnetic fields flow across any junctions, so that no above-mentioned concern on disk-type structures arises.

In 2008, we fabricated a quadrant-type accelerating structure with 18 cells (Fig. 1b), and performed a high-gradient test. The result was that the accelerating gradient (E_acc) was limited to 60 MV/m or lower, and we observed no conditioning effects [5].

We go back to basics on the comparison between disk-type and quadrant-type structures. Disk-type structures have advantages of

- Very smooth surface (typically $R_y \approx 30$ nm), and
- Shallow damage of machining ($< 1\ \mu$m),

while the disadvantages are

- Dozen of disks to be stacked and bonded, and
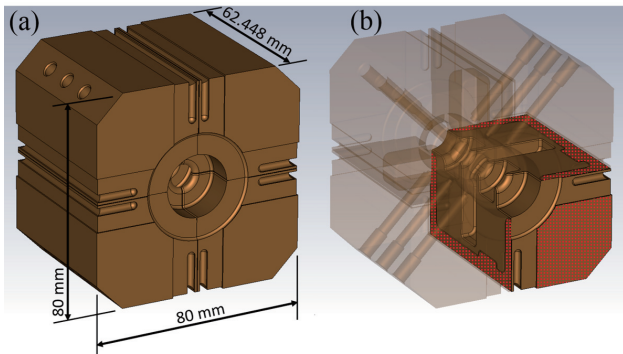- Surface currents associated with magnetic fields flowing across disk-to-disk junctions.

Figure 2: Quadrant-type X-band single-cell structure based on the new ideas. The splotched-red planes indicate reference planes in machining. There are grooves on the surfaces near the mechanical contact between the quadrants to suppress heat diffusion at EBW points.

Quadrant-type structures have advantages of
- No such currents flowing across any junctions, and
- Simple assembly process,

while the disadvantages are
- Not very smooth surface (typically $R_y \approx 1\,\mu$m),
- Deep damage of machining ($\approx 10\,\mu$m),
- Possible virtual leak from quadrant-to-quadrant junctions (see bellow), and
- Field enhancements at the corners of quadrants (see bellow).

We have therefore proposed new ideas on quadrant-type structures to overcome all of the above-mentioned disadvantages, to be explained in the following section.

NEW IDEAS

The ideas proposed in [6] are summarized in this section. The quadrant structure we tested in 2008 (Fig. 1b) was assembled without bonding; the quadrants were just clamped and put in a vacuum chamber for the high gradient test. In such a case, virtual leak from the flat-surface contact between the quadrants might arise due to high fields on the contact. Therefore, as a realistic solution, we make a finite gap of 100 μm between quadrants. ($G = 100\,\mu$m in Fig. 3).

As for the field enhancements at the corners of quadrants, we start at a concave structure parametrized as in Fig. 3, where Δ corresponds to mis-alignment plus machining error of quadrants. In such structure, fields are enhanced as in Fig. 4 for example. Local fields can be calculated with high accuracy by numerical computations in a stochastic approach [7]. Field enhancement factors, calculated with such method, are shown in Fig. 5 [8], where field enhancement factor is defined as a ratio of the maximum field strength around the concave structure and the reference field strength in the case of no concave structure. It should be emphasized that there is a minimum value among the field enhancement factors, that is 1.23 in the case of $G = 0$ and $\Delta = 0$, which is independent of R. Therefore, we should allow 20 to 30 % enhancement of fields. From Fig. 5, it is found that R should
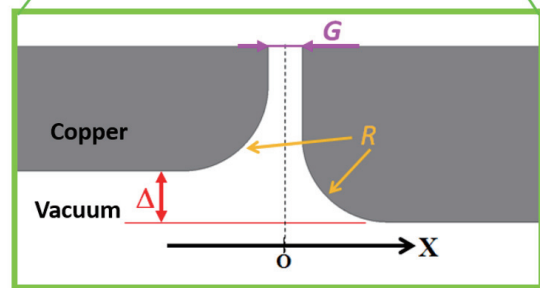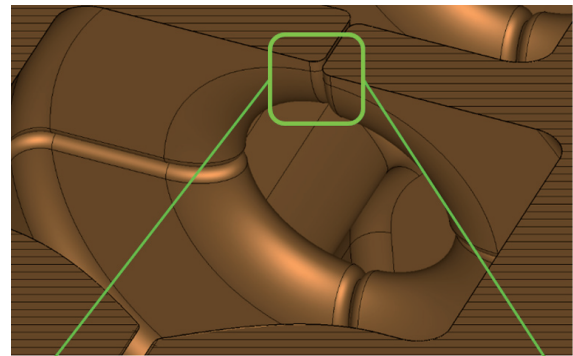

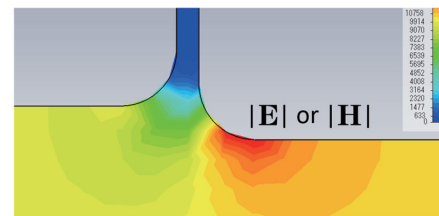Figure 3: Parametrization of a concave structure.

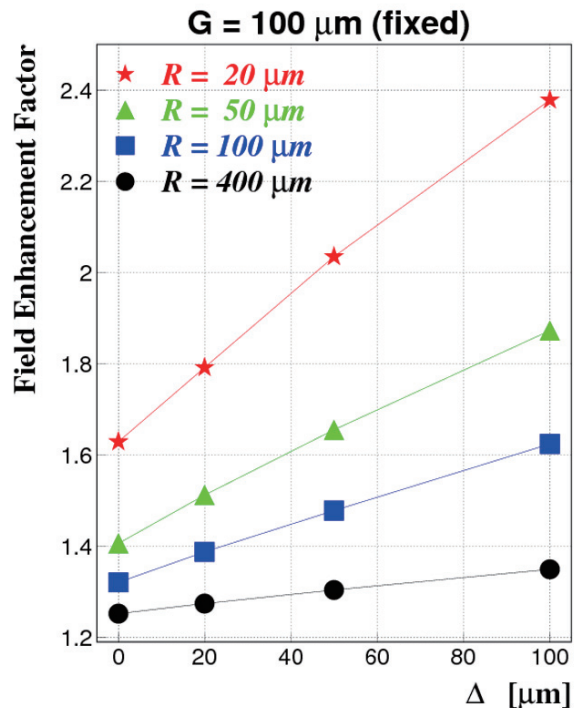Figure 4: Example of enhanced fields at a concave.

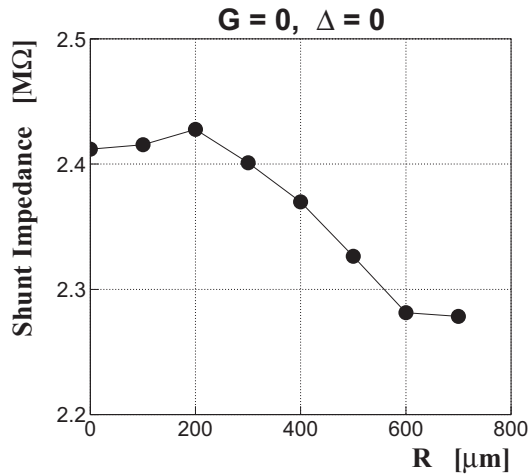Figure 5: Field enhancement factors for the geometry in Fig. 3.

Figure 6: Shunt impedance as a function of R in the case of $G = 0$ and $\Delta = 0$ for the X-band single-cell structure described in [6].
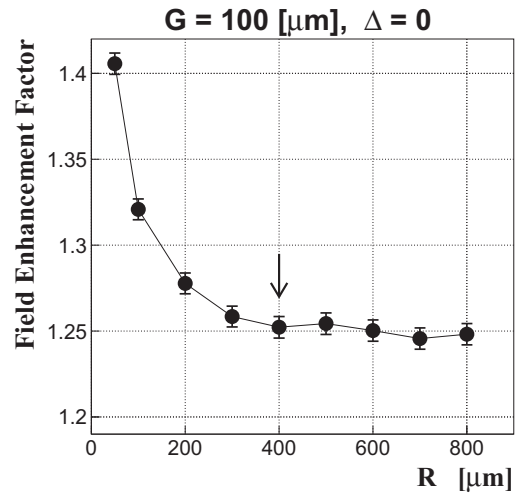

Figure 7: Field enhancement factor as a function of R in the case of $G = 100 \, \mu m$ and $\Delta = 0$ for the geometry in Fig. 3. The arrow indicates our selection on R.
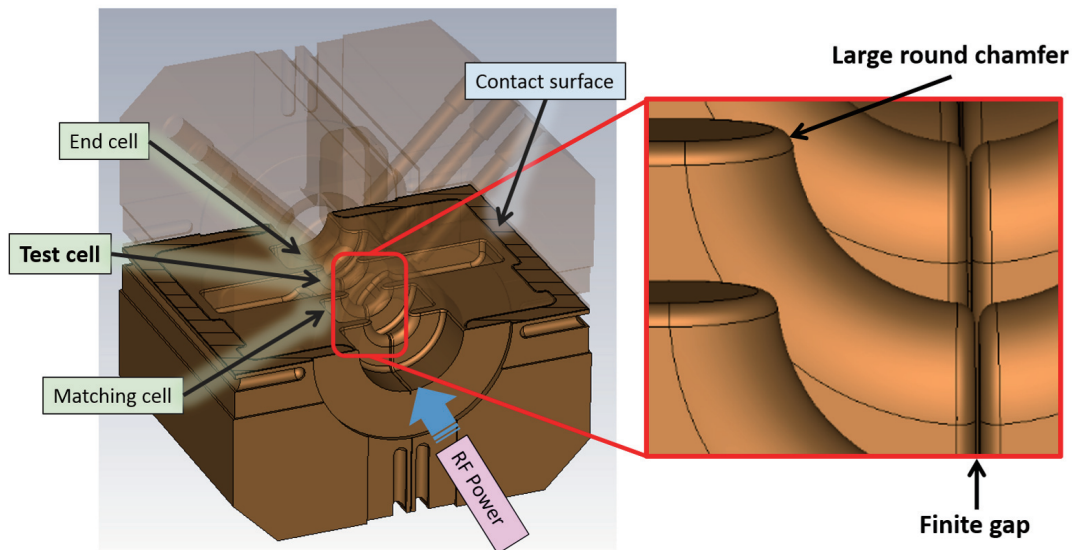

Figure 8: Schematic diagram of the X-band single-cell structure designed based on the new ideas to overcome the disadvantages of quadrant structures. Mechanical contact areas are shown in hatching.

be as large as possible; the enhancement is about 30 % even if $\Delta = 100 \, \mu m$ in the case of $R = 400 \, \mu m$. However, large R decreases the shunt impedance of the accelerating mode as shown in Fig. 6. Based on the R dependence of the shunt impedance and field enhancement factor (Fig. 7), we have determined the optimum value of R to be $400 \, \mu m$ for $G = 100 \, \mu m$ [9]. If we adopt a larger gap ($G > 100 \, \mu m$), we need a larger R, leading to a lower shunt impedance.

As for the surface roughness by milling, we will apply electro-polishing to quadrants after final machining in order to have smoother surface with a target of $R_a \approx 10 \, nm$.

Figure 8 explains the above new ideas schematically.

Figure 9 shows an electromagnetic field of the accelerating mode with an operation frequency of $f_{acc} = 11.424 \, GHz$. This TM mode corresponds to π-mode, one of the three modes in the three-cavity system. The other two modes, corresponding to 0-mode and $\pi/2$-mode, have frequencies about 90 MHz and 140 MHz lower than f_{acc}, respectively. Here we have to pay attention on TE modes, which could have mode frequencies close to f_{acc} because of the $100 \, \mu m$ gap between the quadrants. Actually, there is a significant TE mode, as shown in Fig. 10, with a mode frequency close to f_{acc}. Therefore, in our new design, the shape of the mechanical contact is slightly modified, as shown in Fig. 11. Figure 12 shows how the TE mode frequency changes as the parameter Δ (defined in Fig. 11) changes. Finally, we have adopted $\Delta = 3 \, mm$. As a result, there are no significant effects of TE modes in a frequency range of $f_{acc} \pm 200 \, MHz$.
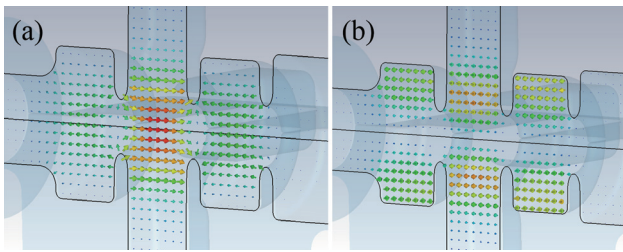
Figure 9: Electromagnetic field of the accelerating mode to be used in high gradient tests. (a) Electric-field vectors. (b) Magnetic-field vectors.
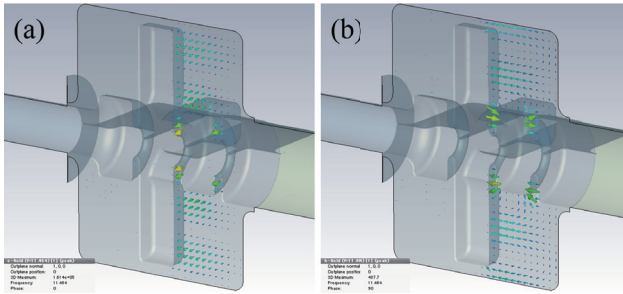

Figure 10: Electromagnetic field of the TE mode with a mode frequency close to f_{acc}. The unloaded quality factor of this mode is 167.
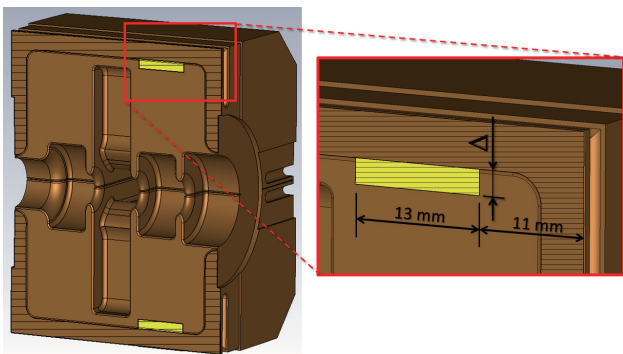

Figure 11: Mechanical contact areas to be added, shown in yellow. The parameter Δ is defined in this figure.

Figure 12: Simulation results on the reflection coefficient ($|S_{11}|$) for Δ (defined in Fig. 11) values of 0, 1, 2, and 3 mm with an input RF wave of TE_{11} in the circular duct (ϕ22.86 mm), where the circles indicate calculation points in the frequency domain computation, and 100%IACS electric conductivity (5.8×10^7 S/m) is assumed for the quadrants. The excited mode is shown in Fig. 10, where the input RF wave comes from the right.

FABRICATION PROCESS

The fabrication process consists of the following steps:

1. Ultra-high precision milling to form quadrants from a OFC (class1) bar
2. Electro-polishing (EP)
3. EBW of the quadrants
4. Brazing of beam ports and flanges

Figure 13 shows one of the quadrants of single-cell structure, to be used in high-gradient tests, which were machined in 2013, where achieved surface roughness and profile accuracy are $R_y \lesssim 1\,\mu$m and $\approx 5\,\mu$m, respectively. Figure 14 shows examples of the profile measurements. In the final machining, we used a five-axes milling machine with a ball end mill (ϕ1.5 mm) made of cemented carbide. In the future, we will use a ball end mill made of single-crystal diamond. As for EP, a study to select appropriate conditions
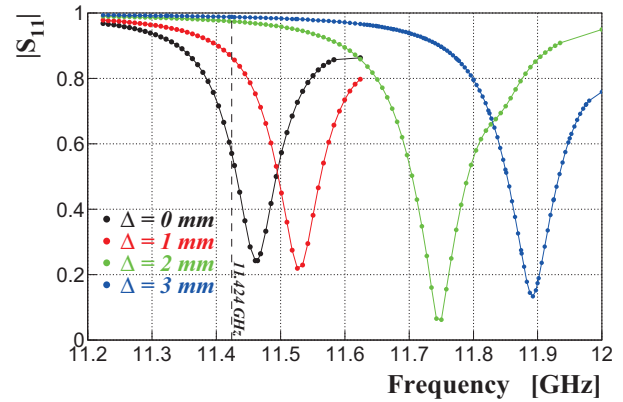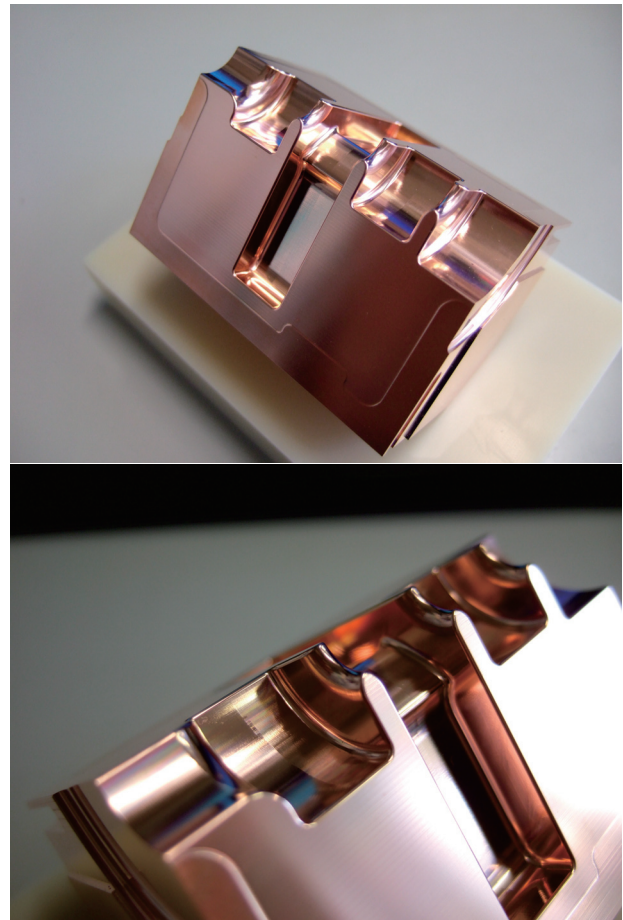

Figure 13: One of the quadrants of single-cell structure, machined in 2013, to be used for high-gradient tests.
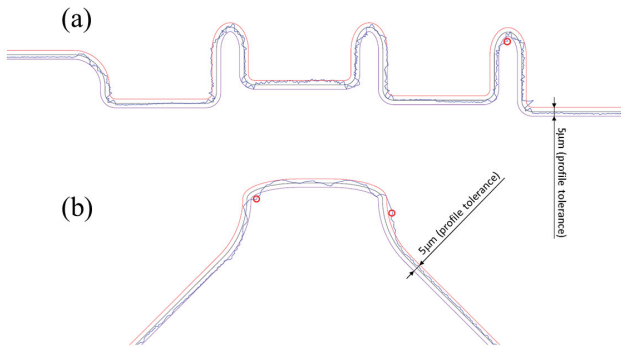
(a)

(b)

Figure 14: Examples of the profile measurements of the single-cell quadrants as shown in Fig. 13. The blue (black) solid lines indicate measured (nominal) profiles. The red circles indicate points outside the profile tolerance of 5 μm (between the red and magenta solid lines). Both of the measured and nominal profiles are shown with respect to the reference planes in machining (splotched-red planes in Fig. 2). (a) Cross section along the beam axis. (b) Cross section of the test cell, perpendicular to the beam axis, where the left and right sides are openings for the HOM waveguides.

is on-going. We assemble the four quadrants into a cavity with EBW for the purposes of both bonding and vacuum sealing. The details of the EBW is described in the next section. The brazing of beam ports and flanges could be replaced by EBW finally in the future so that no high temperature processes are used, making it possible to fabricate the structure made of only hard copper(-alloy) which is strong against metal fatigue due to high surface currents [10].

EBW TEST

We have performed a EBW test using mockups as shown in Fig. 15. Table 1 shows our selection of the EBW conditions, with which we performed the EBW test. The EBW process consists of the followings steps:

1. Tack EBW on the front and back surfaces,
2. Final EBW on the front and back surfaces,
3. Final EBW on the top and bottom surfaces, and
4. Final EBW on the side surfaces.

Before, after, and during the above EBW process, we measured 3D positions of some points on the surfaces of each quadrant, and calculated lengths of line segments, in the longitudinal (beam) and transverse directions, as shown in Fig. 16. Figure 17 shows changes of the line-segment lengths before, after, and during the EBW process. It has been found that the changes are small, < 5 μm, in the longitudinal direction (within the machining tolerance on the inner surfaces of the quadrants), while the changes in the transverse directions are pretty large; the average shrinkage is about 35 μm before the brazing, and 15.8 μm after the brazing. The shrinkage change from $\approx$ 35 μm to 15.8 μm in the transverse directions is a result of stress release by the brazing (BAu 35/65, 1010 degC). If we assume that such shrinkage in the transverse directions is attributed to shrinkage only at the mechanical contact areas, and there is no de-

formation elsewhere, we can estimate a corresponding frequency change to be +12 MHz in f_{acc}. Although this frequency change of 12 MHz is still within the tuning range, the shrinkage of 15.8 μm is taken into consideration in designing the quadrants machined in 2013 (Fig. 13).
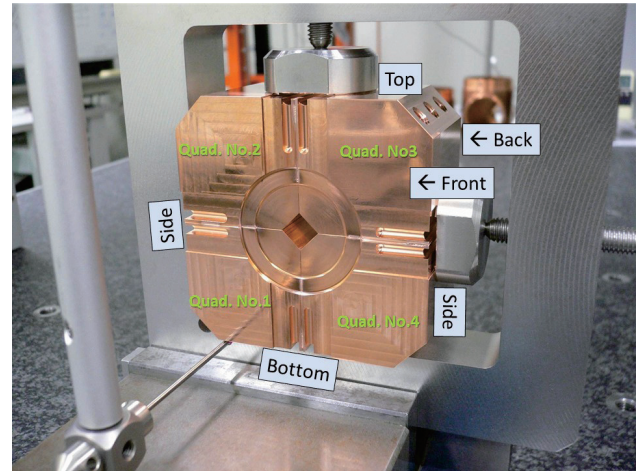

Figure 15: Mockup quadrants for the EBW test, made of OFC, with the inner surfaces simplified. In this photography, 3D positions on the surfaces are being measured after tack EBW on the front and back surfaces.

Table 1: Selected conditions for the EBW.

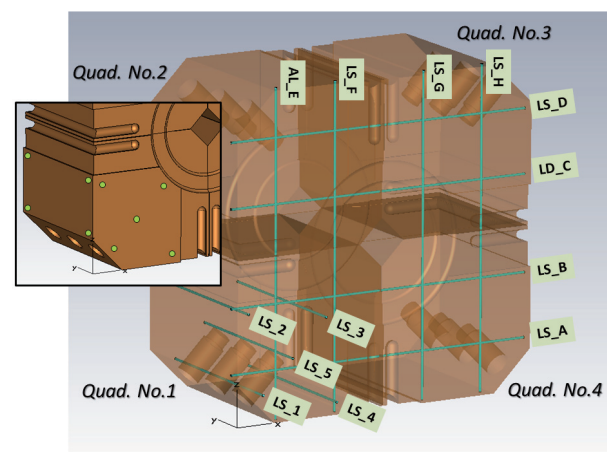|		
Cathode voltage	150	kV
Beam current	10	mA
Spot size (near the groove)	$\approx$ 2 in diameter	mm
Spot size (off the groove)	$\approx$ 1 in diameter	mm
Table speed in the tack EBW	5.8	mm/s
Table speed in the final EBW	4.5	mm/s

Figure 16: Definition of line segments. 3D positions of the endpoints on the surfaces of the mockup quadrants (shown in the inserted figure as green circles for Quad. No.1) were measured. "Quad." means a quadrant. LS_1 to 5 are defined also for Quad. No.2 to No.4 with rotational symmetry. LS_A to H are defined 3 mm away from the font or back surface.

Figure 18 shows the mockup quadrants after the EBW. No vacuum leak higher than 3×10^{-10} Pa m^3/s has been confirmed by a leak test.

Figure 19 shows measured line-segment lengths in the transverse directions, which means that the mis-alignment plus machining error of the mockup quadrants is within ± 10 μm, and the shrinkage by the EBW is uniform, i.e. no deformation on the outer surfaces.
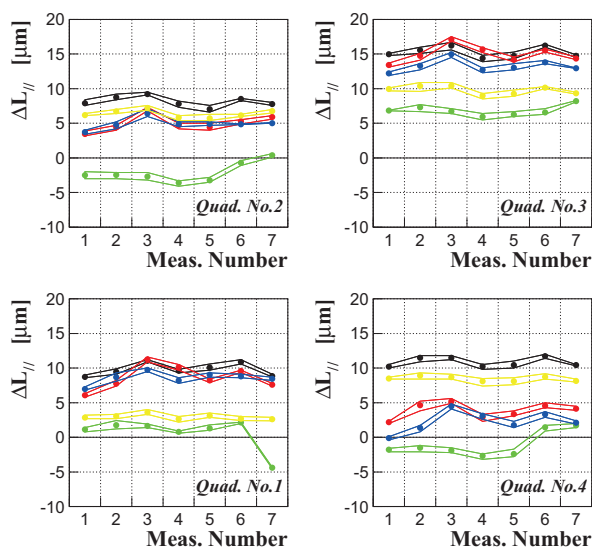
(a) Longitudinal direction. The black, red, green, blue, and yellow plots are measurements for LS_1, 2, 3, 4, and 5, respectively. The plot at the measurement number of 7 for LS_3 on Quad. No.1 is a mis-measurement including a micro scratch on the surface.
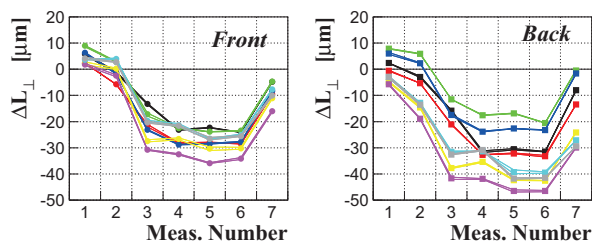
(b) Transverse directions. The black, red, green, blue, yellow, magenta, light blue, and gray plots are measurements for LS_A, B, C, D, E, F, G, and H, respectively.

Figure 17: Changes of the lengths of the line segments, defined in Fig. 16, before, after, and during the EBW process. $\Delta L_{//}$ ($\Delta L_{\perp}$) indicates a measured length minus the design in the longitudinal (transverse) direction. The measurement number indicates each step in the EBW process, 1: Before starting the EBW, 2: Just after the tack EBW on the front and back surfaces, 3: Just after the EBW on the front and back surfaces, 4: Just after the EBW on the top and bottom surfaces, 5: Just after the EBW on the side surfaces, 6: Just after additional machining for brazing of the ports, and 7: Just after brazing of the ports.
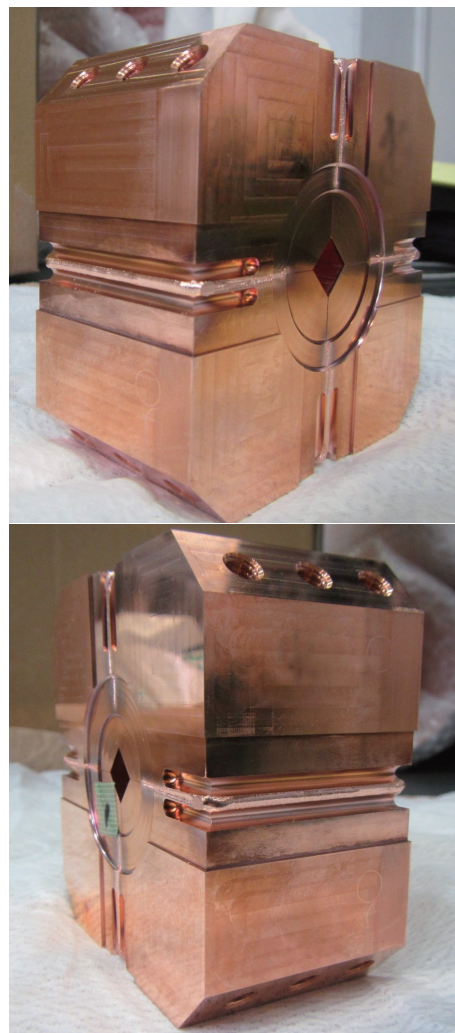

Figure 18: Mockup quadrants after the EBW.

SUMMARY AND CONCLUSIONS

Based on the new ideas to overcome all of the disadvantages of quadrant-type structures, we have designed and machined a quadrant-type single-cell structure to be used for high-gradient tests. We have also shaped a fabrication process, including EBW. The test of EBW for the purposes of both bonding and vacuum sealing of the quadrants was successfully performed, and we have found that the average shrinkage in the transverse directions is 15.8 μm, corresponding to +12 MHz in f_{acc}, for the selected EBW conditions, and such shrinkage is uniform; the quadrants have no deformation on the outer surfaces.

Front (x 200)

(a) Front side.

Back (x 200)
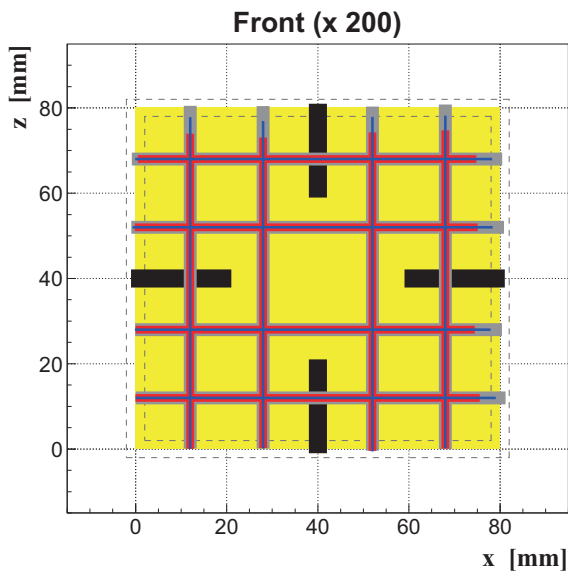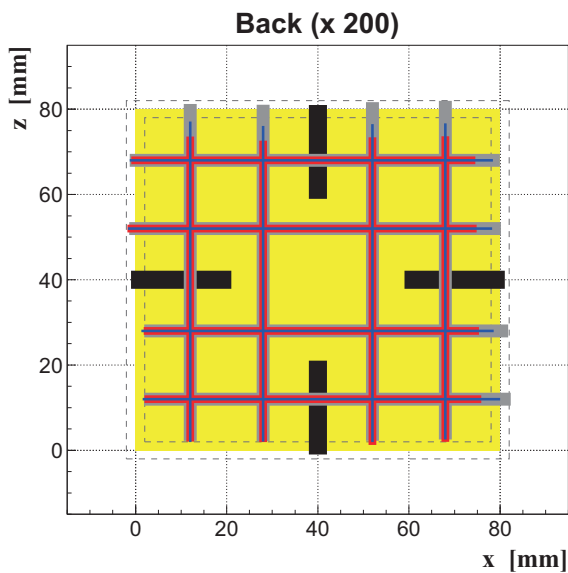
(b) Back side.

Figure 19: Measured line segments in the transverse directions. The yellow areas indicate the design, and the gray dashed lines indicate ± 10 μm tolerance magnified 200 times in this figure. The black bars are EBW beads. The gray bars, red bars, and blue lines indicate measurements before the EBW process, just after the EBW process, and after the brazing, respectively. All of the measurements are shown with the differences from the design magnified 200 times in this figure. Cartesian coordinates (x, y, z) are defined in Fig. 16.

REFERENCES

[1] V. A. Dolgashev, S. G. Tantawi, C. D. Nantista, Y. Higashi and T. Higo, "Travelling wave and standing wave single cell high gradient tests," SLAC-PUB-10667, 2004.

[2] M. Aicherer, CERN EDMS, "TD18 post-mortem SEM observation:Update," presentation at CERN, 10 Nov. 2010.

[3] V. A. Dolgashev, S. Tantawi, Y. Higashi, B. Spataro, "Geometric Dependence of Radio-Frequency Breakdown in Normal Conducting Accelerating Structures," Appl. Phys. Lett. 97, 171501, 2010.

[4] F. Wang, C. Adolphsen and C. Nantista, "Performance Limiting Effects in X-Band Accelerators," Phys. Rev. ST Accel. Beams **14**, 010401, 2011 [Addendum-ibid. **15**, 120402 (2012)].

[5] T. Higo, "KEK activities on CLIC X-band Accelerating Structures," presented at the mini-workshop on CLIC X-band structure R&D at THU, 2010 (http://indico.cern.ch/event/89913/).

[6] T. Abe, Y. Higashi, Y. Arakida, T. Higo, S. Matsumoto, T. Shidara and T. Takatomi, "Quadrant-Type X-Band Single-Cell Structure for High Gradient Tests," in Proceedings of the 9th Annual Meeting of Particle Accelerator Society of Japan, August 2012 (Paper ID: THPS095).

[7] T. Abe, "Study of Surface Field Enhancements due to Fine Structures," in Proceedings of the 8th Annual Meeting of Particle Accelerator Society of Japan, August 2011 (Paper ID: TUPS086).

[8] The results are obtained for a boundary with two parallel plates. Using a circular boundary, the results are almost the same [6].

[9] The optimum value of R might depend on the geometry of the accelerating structure.

[10] V. Dolgashev, S. Tantawi, A. Yeremian, Y. Higashi and B. Spataro, "Status of High Power Tests of Normal Conducting Single-Cell Standing Wave Structures," Conf. Proc. C **100523**, THPEA060 (2010).